Robotica (2013) volume 31, pp. 465–478. © Cambridge University Press 2012
doi:10.1017/S0263574712000446

Indirect force control development procedure

Tomasz Winiarski* and Adam Woźniak

Institute of Control & Computation Engineering, Warsaw University of Technology, Warsaw, Poland

(Accepted July 18, 2012. First published online: August 16, 2012)

SUMMARY

Addition of extra sensors, especially video cameras and force sensors, under control of appropriate software makes robotic manipulators working in factories suitable for a range of new applications. This paper presents a method of manipulator indirect force control development, in which the force set values are specified in the operational space and the manipulator is equipped with a force sensor in its wrist. Standard control development methods need the estimation of parameters of the detailed model of a manipulator and position servos, which is a complicated and time-consuming task. Hence, in this work a time-efficient hybrid procedure of controller development is proposed consisting of both analytical and experimental stages: proposal of an approximate continuous model of a manipulator, experimental determination and verification of its parameter values using the resonance phenomenon, continuous regulator development, and digitization of the regulator.

KEYWORDS: Manipulator control; Indirect force control; Controller development.

1. Introduction

Although traditional industrial robots are position-controlled, the new challenges that robot manipulators face require gentle contact between the manipulator and the environment and this necessitates appropriate force control. If the model of the environment is geometrically uncertain,[4] the active force control mechanism should be chosen, where, in opposition to passive approach, the force is measured (typically in the manipulator end-effector) and a force control loop is implemented. Some of the force control tasks are industrial in nature: deburring, polishing, or grinding; others, such as the ones performed by the haptic devices,[14] are executed by medical[30] or space exploration robots (both under water and in the outer space). Finally, service robots,[16,22] which operate in human-oriented environment, require the same senses as humans, especially tactile, hence force control is also utilized there.

For the purpose of intuitive and time-efficient task definition, an operational space[17] or similar task frame[8] was introduced. Most of the scientific force-controlled systems use manipulators with torque-controlled joints and known inverse dynamic problem solution.[9,17] Industrial manipulators that exist in significant numbers in laboratories and factories, with properly tuned proportional-integral-derivative (PID) controllers of joints position,[5] are also suitable to perform particular tasks of service robots when equipped with proper sensors, e.g., force sensors mounted in the wrist.[36] The force control law can be defined in the operational space taking into account the manipulator and the environment properties gathered before task execution,[21] or alternatively computed on-line.[26] The second approach is suitable for service robots, which perform manipulation in the unstructured environment.

1.1. Direct and indirect force control

In general, manipulation requires three behaviors: contact with the environment, unconstrained position motion, and intermediate or transitional behavior that can be commanded for each of the directions of the operational space.[21,36] The task specified with respect to the end-effector frame (Fig. 1) has to be executed by the controller of the robotic manipulator. There are two fundamental approaches: direct force control and indirect force control.[31] Here we concentrate on the latter.

The indirect force controller (Fig. 2) is a manipulator controller that has two loops. The external one is force-controlled, and the internal one is position-controlled.

For the indirect force control, the operational space controller produces the desired velocity $\dot{X}_d$ represented in the operational space. This velocity is transformed into desired position θ_d in configuration space by the coordinate transformation block. The configuration space controller commands the robot, i.e., motors, to attain position θ_d.

The direct force controller also has two loops, but contrary to the indirect force controller the internal loop is torque-controlled. The purpose of the internal loop is to achieve desired torque, for each of the joints, produced by external controller taking into account the manipulator dynamics, under the condition that dynamics is known.

The indirect force control is often built on top of a typical industrial manipulator controller, which makes it easier to develop than direct force control. Especially for some of the robots, e.g., IRb6 industrial manipulator used in the experiments presented further, in practice it is very difficult to accurately model friction occurring in its mechanisms,[29] which makes obtaining the full dynamic model needed by direct force control very difficult.

Pure force control methods implemented as the indirect force control are often termed as the admittance control or the explicit control. A short overview of these methods is

* Corresponding author. E-mail: tmwiniarski@gmail.com

https://doi.org/10.1017/S0263574712000446 Published online by Cambridge University Press

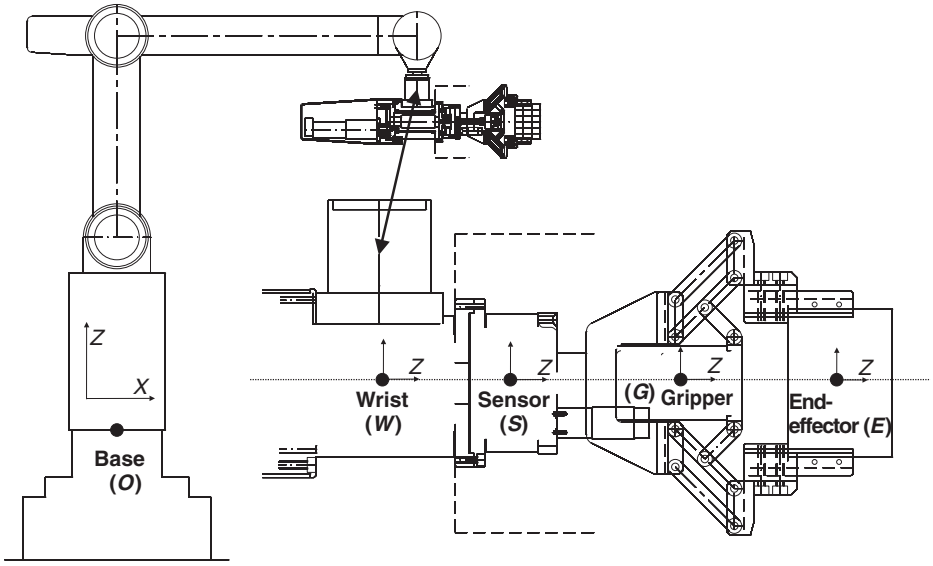


Fig. 1. Manipulator structure and coordinate systems affixed to it: O – base, W – wrist, S – force sensor, G – gripper (its origin is located at the gripper mass center and the orientation is the same as that of frame W), E – end-effector (operational space frame).

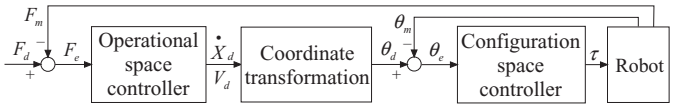


Fig. 2. Indirect force control. Here and in the following figures, F_d – desired force (operational space), F_m – force measured by the force sensor (transducer) located near the manipulator wrist with the gravitational force removed (operational space), F_e – force error (operational space), $\dot{X}_d$ – desired velocity (operational space, continuous time domain), V_d – desired velocity (operational space, discrete time domain), θ_d – desired position (configuration space), θ_m – measured position (configuration space), θ_e – position error (configuration space), τ – control for the motors produced by the configuration space controller (i.e., desired voltage, pulse-width modulation (PWM) duty cycles, or desired current).

presented in ref. [31]. Some of the works present the methods of computing admittance controller parameters.[15,23] Others describe the utilization of active admittance control in haptic coupling.[24]

1.2. Controller development

The simplest control law that can be implemented in the system presented in Fig. 2 is the proportional control law, which in the discrete case can be written as

$$V_d{}^{\iota} = k(F_d^{\iota} - F_m^{\iota-1}), \tag{1}$$

where k is the proportional gain, ι is the current time instant, and $\iota - 1$ is the previous time instant. This law implements discrete P controller that, in the continuous version, was the base for the first motion controllers of industrial machines.[7] The proportional control law can be naturally extended by introducing memory, e.g., in one of the variants, by taking into account the control history:

$$V_d^{\iota} = h(V_d^{\iota-1}) + k(F_d^{\iota} - F_m^{\iota-1}), \tag{2}$$

where h is a proportional factor. The practical implementation of this algorithm was used in a similar form in the discrete control law developed in this work (Section 4.1). The main problem is determination of controller parameters. Historically first is strictly experimental,[7] where a series of experiments are performed on a real object, for different sets of control parameter values. These parameters are chosen to attain the best visible performance of the system. Unfortunately, this method is time-consuming, and, in addition, the plant can be damaged during the experiments. Hence, a number of formal methods were proposed based on the plant's model, e.g., frequency domain methods[19] or robust control methods.[11]

In control theory, linear, continuous models are clear, intuitive, and quite easy to analyze in opposition to the non-linear and discrete models. In the following considerations the approximation of the complicated analog-discrete manipulator model is obtained by the proposed linear, continuous methods. The approach is good enough to perform reliable and valuable analysis.

The properties of a dynamic system described by the transfer function $G(s)$, its phase, and amplitude Bode characteristics can be represented by two functions. The first function $\mathcal{L}(G, f)$ produces the gain in the logarithmic scale for the assumed transfer function and frequency. The second $\mathcal{P}(G, f)$ returns the phase shift in degrees. In the following, the simplified, single argument notation ($\mathcal{L}(G)$ and $\mathcal{P}(G)$) will be used, where the particular resonant frequency value $f = f_r$ is considered (Section 3). Similarly, to simplify the notation, the product of transfer functions is represented in the following form:

$$G_1(s)\, G_2(s) = G_{12}(s). \tag{3}$$

1.3. Indirect force controller development procedure

In this paper we present a new hybrid procedure to obtain the parameters of an indirect force controller of a robotic manipulator. We used an approximate continuous model of the manipulator and position servos as a part of the

https://doi.org/10.1017/S0263574712000446 Published online by Cambridge University Press

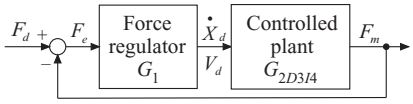


Fig. 3. Control system.

control system (Section 2) instead of a detailed model to obtain a simple and time-efficient way to develop force regulator. The parameters of this approximate model were determined (Section 3) in the experiments and simulations were performed on the closed loop system with a proportional regulator as in Fig. 3. The procedure utilizes the resonance phenomenon, while the manipulator safely attains a suitable resonance. Then, taking into account the identified controlled plant model, the continuous force regulator itself was developed to exhibit as low damping (the relationship of the force error and the resultant velocity) as possible, while the whole system remained stable. The first-order lag element was chosen as the regulator to perform low pass filteration, instead of PI regulator, commonly used in force feedback,[31] for the reasons presented in Section 4. Subsequently, further experiments were performed to verify whether the developed controller is suitable to control the real plant (Section 4). To achieve this, the regulator was transformed into discrete form (Section 4.1) followed by the evaluation of the procedure (Section 5). Finally, the regulator parameter adaptation method based on contact stiffness is presented and experimentally verified in Section 6.

There are six directions in the operational space (three linear and three angular). The directions of motion in the task space are generally decoupled for the robotic manipulator driven by geared motors that are controlled by the individual position servos, e.g., IRb6 used in the experiments. Hence, the force regulator, as it is presented in the following part of this paper, was developed for a single direction of the task space. Each direction of motion in the task space is controlled by a separate force regulator. It should be noted that these motion directions do not coincide with the motions caused by single actuators.

2. Control System

The indirect force controller in Fig. 2 can be presented as in Figs. 3 and 4 to illustrate the proposed controller development procedure description. Here, the control loop is built for a single degree of freedom in the operational space (the end-effector frame E in Fig. 1). Both force controller and controlled plant models are assumed as continuous and linear, hence represented by transfer functions.

The presented control structure is an instance of the so-called cascade control well known for process control community.[20] Following is the rationale for using this structure: The well-tuned inner loop of Fig. 2 (starting from coordinate transformation and ending on measurement of position) has for rigid manipulator nearly linear dynamics, which in practice can be modeled as second-order lag element.[10] From the outer loop controller (operational space controller) point of view, the inner loop (controlled plant in Fig. 3) is a linearized system.[5,9,12] As a consequence, when we properly identify linear model of our controlled plant, we are able to tune linear operational space controller well.

The force regulator in Fig. 3, the new element that has not appeared up to now, computes the control $\dot{X}_d$ on the basis of the force error F_e. In the majority of the following experiments a simple proportional relation is assumed: $G_1'(s) = \frac{1}{B_p}$. Then, the first-order lag element is proposed as the regulator: $G_1''(s) = \frac{\frac{1}{B_p}}{\frac{M_p}{B_p}s+1}$, where B_p is the regulator damping, and M_p is the regulator inertia. The transfer function $G_1''(s)$ is more general, thus we assume that in general $G_1(s) = G_1''(s)$, then in particular, for $M_p = 0$, $G_1(s) = G_1'(s)$.

The controlled plant in Fig. 3 is the manipulator represented by the lumped transfer function $G_{2D3I4}(s)$, i.e., servomotors, gears and links, force sensor and tool. The same controlled plant model is presented in details in Fig. 4. It takes into account the manipulator construction and presents signals in a form suitable for further analysis. Moreover, the forms of particular transfer functions are derived experimentally and are presented in Section 3. This model is constructed as a relationship between Laplace transforms of input and output signals by treating all components as linear.

In the following signals and elements that have not appeared up to now are described, starting from the left side of the schema in Fig. 4.

- $\dot{X}_m$: Measured velocity of the end-effector. In the experiments this velocity is computed using joint positions, subsequently transformed into the end-effector position by solving the directo kinematics problem: $\dot{X}_m^\iota = \frac{X_m^\iota - X_m^{\iota-1}}{\Delta t}$, where X_m^ι is the end-effector position in current time instant, $X_m^{\iota-1}$ is the end-effector position in the previous time instant, Δt is the sampling time.
- $\ddot{X}_m$: Measured acceleration of the end-effector is computed in the following way: $\ddot{X}_m^\iota = \frac{\dot{X}_m^\iota - \dot{X}_m^{\iota-1}}{\Delta t}$, analogically to the measured velocity $\dot{X}_m$.
- $\ddot{X}_r$: Real acceleration of the end-effector. This value cannot be directly measured in the experiments, it can be indirectly estimated, e.g., by simulation.
- $\dot{X}_r$: Real velocity of the end-effector. This value also cannot be directly measured in the experiments, it can be, e.g., integrated from $\ddot{X}_r$.

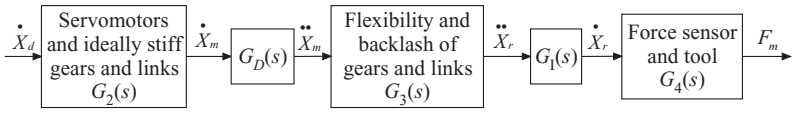


Fig. 4. Controlled plant.

https://doi.org/10.1017/S0263574712000446 Published online by Cambridge University Press

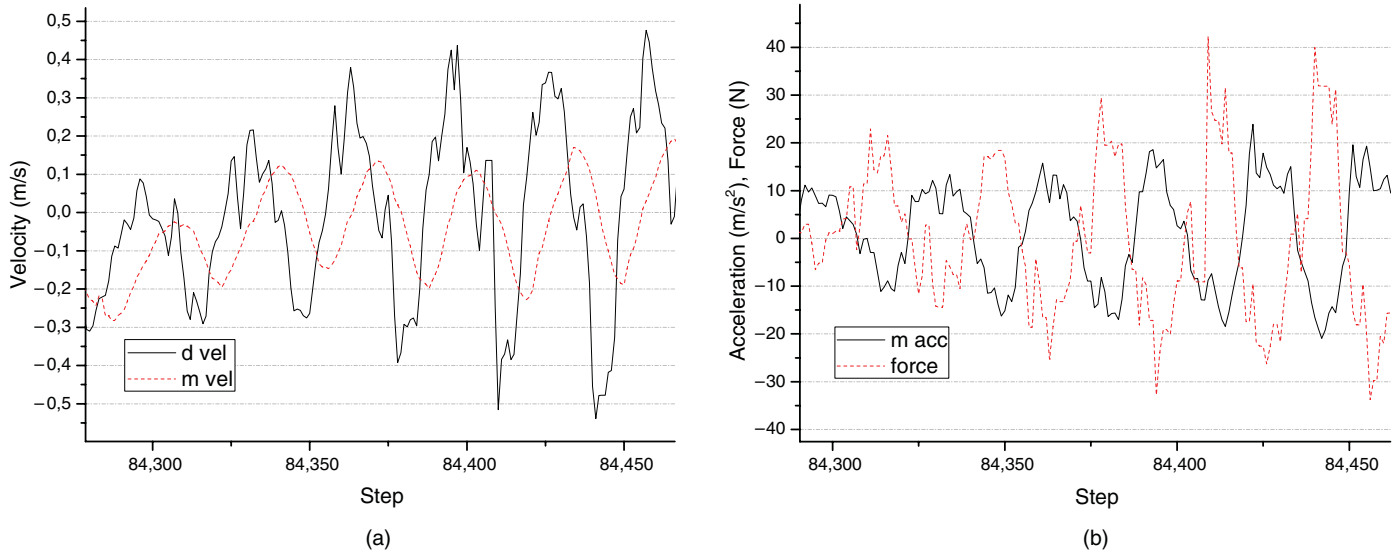


Fig. 5. (Colour online) Results of identification experiments, where here and in the following plots step = 0.002 s. (a) d vel – $\dot{X}_d$, m vel – $\dot{X}_m$; (b) m acc – $\ddot{X}_m$, force – F_m.

- Servomotors and ideally stiff gears and links: The position servos containing motors and ideally stiff gears and links. It should be noted that to move along a single axis in the operational space generally several joints have to move simultaneously. For this, direct and inverse kinematic problem solvers need to be used. After analysis of the relationship between the desired velocity $\dot{X}_d$ and the measured velocity $\dot{X}_m$ obtained in the experiments, it is deduced that a second-order lag element $G_2(s) = \frac{1}{(T_a s+1)(T_b s+1)}$ is a good approximation of a system producing such a large phase shift.
- Differentiation: Represented by the transfer function $G_D(s) = s$.
- Flexibility and backlash of gears and links: In practice, the measured acceleration $\ddot{X}_m$ and the real acceleration $\ddot{X}_r$ differ significantly in phase. This is caused by the dynamic properties of a particular manipulator, e.g., transmission compliance and backlash. The measured acceleration is derived from encoder measurements. Encoders are fixed to the motor shafts. All other mechanical elements, exhibiting flexibility and backlash, are also fixed to those shafts. Thus, the response at the end-effector is delayed in relation to the encoder-based measurement. Taking into account the preliminary experiments, it is assumed that $\ddot{X}_r$ is delayed with respect to $\ddot{X}_m$ by a particular time T_d, what can be represented by the transfer function $G_3(s) = e^{-sT_d}$, i.e., transport delay.
- Integration: Represented by the transfer function $G_I(s) = \frac{1}{s}$.
- Force sensor and tool: The general force is measured by a force sensor (dedicated transducer) located between the manipulator wrist and the tool. The mass of the tool cannot be neglected, because the force sensor measures not only the contact forces (between the manipulator end-effector and the environment), which are interesting from the control point of view, but also gravitational and inertial forces caused by the tool. In the presented model the mechanical impedance relates the real velocity of the end-effector and the measured force: $Z(s) = Ms + B + \frac{K}{s}$, where M is the tool mass, B is the contact damping and K is the contact stiffness. Thus, the whole element is represented by the transfer function $G_4(s) = Z(s)$. When the end-effector is in contact with the environment, two parameters, namely B and K, depend on the manipulator and the environment properties. In case of no contact, B and K should be treated as zero.

Table I. Control system model parameter symbols and their units.

Force regulator		Servomotors, gears, links			Force sensor, tool						
B_p	M_p	T_a	T_b	T_d	M	B	K	f	ω	$\mathcal{L}(G)$	$\mathcal{P}(G)$
$[\frac{\text{kg}}{\text{s}}]$	[kg]	[s]	[s]	[s]	[kg]	$[\frac{\text{kg}}{\text{s}}]$	$[\frac{\text{kg}}{\text{s}^2}]$	[Hz]	$[\frac{1}{\text{s}}]$	[dB]	[°(deg)]

The transfer functions $G_D(s)$ and $G_I(s)$ are introduced for the purpose of clearer presentation of the relationship between signals $\dot{X}_m$, $\ddot{X}_m$, $\ddot{X}_r$, and $\dot{X}_r$, in particular the delay between $\ddot{X}_m$ and $\ddot{X}_r$.

It should be noted that the signals represented in Figs. 3 and 4 are Laplace transforms. In the following the same symbols are used to denote time domain signals and their Laplace transforms, in particular in the plots obtained during the experiments, e.g., in Fig. 5, and simulation, e.g., in Fig. 6. Their distinction is obvious – based on the context.

3. Identification of the Controlled Plant Parameters

The force regulator and the controlled plant model parameter symbols and their units are presented in Table I. The values of controlled plant parameters are obtained in the following manner:

- T_a, T_b – Time constants of the second-order lag element are chosen to obtain correspondence between the measured velocity $\dot{X}_m$ and the desired velocity $\dot{X}_d$.

https://doi.org/10.1017/S0263574712000446 Published online by Cambridge University Press

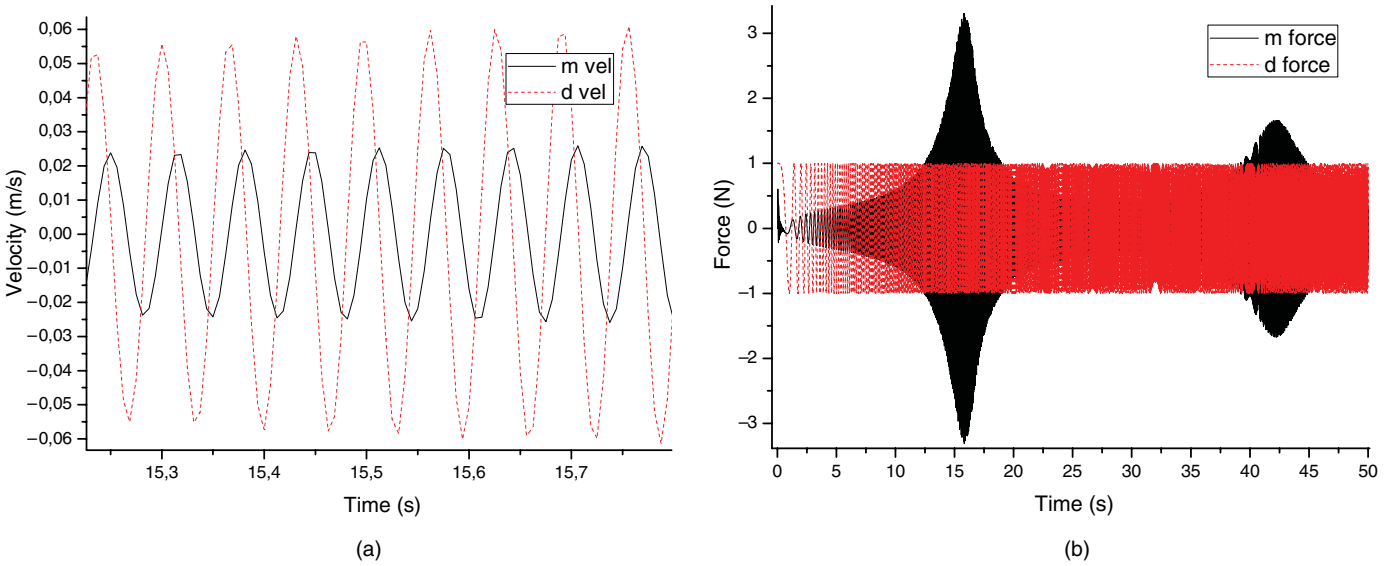


Fig. 6. (Colour online) Simulation results for identification phase (frequency increases with time). (a) d vel – $\dot{X}_d$, m vel – $\dot{X}_m$; (b) d force – F_d, m force – F_m.

- T_d – The transport delay relating the measured velocity $\dot{X}_m$ and difficult to measure real velocity $\dot{X}_r$. The T_d relates measured acceleration $\ddot{X}_m$ and the difficult to measure real acceleration $\ddot{X}_r$. Fortunately, $\ddot{X}_r$ can be obtained during the experiments, where there is no contact between the end-effector and the environment (for the mass M is known, and both damping B and stiffness K are zero). Then $\ddot{X}_r = \frac{F_m}{M}$, because if there is no contact, F_m is simply an inertial force.
- M – This mass is equal to the value of the mass of the tool affixed to the force transducer. This parameter can be measured quite accurately in the experiment.[36]
- B – Damping is noticeable (non-zero) in the contact situation, e.g., when the operator holds the tool.
- K – In the following experiments this stiffness is constantly set to zero, because all of the contact properties are assumed to be modeled by damping B.

The force regulator parameters are set directly:

- B_p – Force regulator damping is a consequence of the force regulator implementation (Section 4.1), hence it is known accurately.
- M_p – Force regulator inertia, similar to the force regulator damping, is a consequence of the force regulator implementation (Section 4.1), hence it is known accurately.

3.1. Identification procedure

The experiments were performed on a real robotic system containing an IRb6 manipulator with research-oriented motor controllers.[27] It was controlled by an `MRROC++` based control system.[3,34] `MRROC++` is a robotic programming framework implemented on the basis of formal considerations. It utilizes an agent approach for structuring the control system, and a transition function approach for defining agent behaviors.[32]

In these particular experiments, the model was identified for a single direction in operational space. The motion was performed along the single axis of the base frame parallel to the floor surface. MATLAB and Simulink were used for analysis and simulation. The analysis was performed for the frequencies from several to 250 Hz because, taking into account the sampling theorem, the maximal theoretical frequency of the transmitted signal was 250 Hz for the sampling frequency of 500 Hz that was used in the experimental system.

The transfer function of the closed loop system presented in Fig. 3 is

$$G_Z(s) = \frac{G_{12D3I4}(s)}{1 + G_{12D3I4}(s)} = \frac{G_{1234}(s)}{1 + G_{1234}(s)}. \quad (4)$$

In the experiments performed on the real manipulator, the desired force F_d was set to zero. Hence, the manipulator was compliant, i.e., reacted to the forces acting on the end-effector, and reduced them. During some of the experiments, continuous oscillation occurred for particular resonant frequency f_{r_e}. The force regulator itself was developed to eliminate such oscillations (Section 4). The controlled plant was identified for signal frequencies around the resonant frequency, and the properties of this oscillation was the source of data for the controlled plant model construction and identification of some of its parameter values.

The resonance phenomena can be observed in a system with a positive feedback. In the case of both experiments and simulations, this type of feedback occurred. In the following, the results of experiments and simulations will be presented for particular model parameter values. Two of the parameters, the force regulator damping B_p and the contact damping B, were changed. In the experiments the desired force was zero and the oscillation occurred due to disturbance (e.g., external force or force measurement noise). In simulation, the Bode characteristics of the closed loop system were analyzed to define the frequency of the first, dominant resonance peak. Similarly, it was possible to simulate the system in MATLAB Simulink, where neither disturbance nor measurement noise

https://doi.org/10.1017/S0263574712000446 Published online by Cambridge University Press

was introduced, but the desired force signal was sinusoidal with an increasing frequency. The reason for this was that in simulation the highest gain of the control system $G_Z(s)$ occurred for the frequency, f_{r_s} that corresponded to the resonant frequency, f_{r_e}, where the resonance occurred in the experiments. In the following, the right subscript e corresponds to experiments and right subscript s corresponds to simulation.

A series of experiments and simulations were performed to identify some of the controlled plant model parameter values (Section 3.2) for the system that moved with no contact with the environment. Subsequently those values were tested (Section 5) for the system in contact with the environment. It was done to obtain conformity of resonant frequencies and time graphs of particular signals between the simulation and experiments on real robot. The general procedure consisted of the following three steps:

(1) Experiment execution and data acquisition (the $\dot{X}_d$, $\dot{X}_m$, $\ddot{X}_m$, F_m signals were recorded).
(2) Analysis of the plots based on experimental data leading to the evaluation of properties of the real system.
(3) Selection of simulated model parameters to obtain conformity between the behavior of real robot and the simulation model.

The detailed procedure of the second and third steps was as follows:

(1) The resonant frequency f_{r_e} in the experiment was obtained by analyzing the signal as in Fig. 5(a),

$$f_{r_e} = \frac{n_o}{T_o}, \tag{5}$$

where n_o is the number of oscillations and T_o is the total time of those oscillations. Both quantities were directly obtained from the plot. A significant number of oscillations were considered (at least five) to obtain a good estimation of resonant frequency.
(2) The functions $\mathcal{L}_e(G_2)$ and $\mathcal{P}_e(G_2)$ for the experiments were computed by taking into account the plots, such as in Fig. 5(a),

$$\mathcal{L}_e(G_2) = 20\log\frac{A(\dot{X}_m)}{A(\dot{X}_d)}, \tag{6}$$

where $A(\dot{X}_m)$ is the average amplitude of $\dot{X}_m$ while it was oscillating, and analogically $A(\dot{X}_d)$ is the average amplitude of $\dot{X}_d$ in the same time period. Rough values were obtained from the plots,

$$\mathcal{P}_e(G_2) = 360\frac{T_s}{T_p}, \tag{7}$$

where T_s is the mean time shift of signals $\dot{X}_m$ and $\dot{X}_d$, and T_p is the mean period of oscillation.
(3) Functions $\mathcal{L}_e(G_{3I4})$ and $\mathcal{P}_e(G_{3I4})$ were obtained from the plots such as in Fig. 5(b) in an analogical way just as functions $\mathcal{L}_e(G_2)$ and $\mathcal{P}_e(G_2)$ were obtained.
(4) In simulation the values of B_p, M_p, M, and K were predefined as it was described previously.

Table II. Control system parameter values obtained in the identification phase.

f_{r_e}	f_{r_s}	B_p	M_p	T_a	T_b	T_d	M	B	K
15.1	15.6	70	0	0.004	0.02	0.033	1.3	0	0

	G_1	G_2		G_{3I4}		G_{I4}	G_Z
	exp, sim	exp	sim	exp	sim	sim	sim
$\mathcal{L}()$	−36.9	−6	−7.5	2.3	2.3	2.3	10.5
$\mathcal{P}()$	0	−90	−84	−180	−186	0	−180

(5) The value of T_d was selected to produce conformity between $\mathcal{L}_e(G_{3I4}) \approx \mathcal{L}_s(G_{3I4})$ and $f_{r_e} \approx f_{r_s}$. The values of $\mathcal{L}_s(G_{3I4})$ and $\mathcal{P}_s(G_{3I4})$ can be obtained directly from the corresponding Bode characteristics of the simulated model as in Fig. 8(a). In the verification phase (Section 5) the value of T_d was taken from the identification phase (Section 3.2) and the B parameter was selected to obtain conformity of simulations with the experiments with damped contact (especially resonance frequencies).
(6) The T_a and T_b values were selected to obtain conformity between $\mathcal{L}_e(G_2) \approx \mathcal{L}_s(G_2)$, $\mathcal{P}_e(G_2) \approx \mathcal{P}_s(G_2)$, and $f_{r_e} \approx f_{r_s}$. Values of $\mathcal{L}_s(G_2)$ and $\mathcal{P}_s(G_2)$ can be obtained directly from the Bode characteristics of the simulated model.
(7) Additional functions $\mathcal{L}_s(G_{I4})$, $\mathcal{P}_s(G_{I4})$, $\mathcal{L}_s(G_Z)$, and $\mathcal{P}_s(G_Z)$ were computed in the simulation phase to extend the presentation of the control system model properties. In particular, the simulated Bode characteristic of the transfer function G_Z presents the resonance peaks of the whole system. The simulated Bode characteristics of the transfer function G_{I4} presents the force measurement F_m as a function of the real acceleration $\ddot{X}_r$ and the possible contact properties.

It should be noted that f_{r_s} depends significantly on T_d.

The measurements of the quantities (as in Table II) obtained in the experiments executed on real robot were approximate because they were based on the analysis of signal graphs. The resonant frequency f_{r_e} can be determined relatively precisely, while the gains and phase shifts were approximate. The transfer function G_1 is an exception, because it can be obtained directly from the implementation code and does not require any measurement. On the other hand, the Bode characteristics obtained by simulation are precise, but the controlled plant model is approximate.

3.2. Experiments and simulations

The identification experiments were performed on a system containing a simple proportional force regulator and with no contact between the end-effector and the environment. The goal was to determine the values of some of the parameters of the controlled plant, in particular T_a, T_b, and T_d, to obtain correspondence between the simulation and the experiments performed on real robot.

The graphs in Fig. 5 present the measurements obtained in the experiments. These were used to obtain $\mathcal{L}_e(G_2)$ and $\mathcal{P}_e(G_2)$ from Fig. 5(a), and $\mathcal{L}_e(G_{3I4})$ and $\mathcal{P}_e(G_{3I4})$ from Fig. 5(b). The desired velocity $\dot{X}_d$ plot is noisy, because it was

https://doi.org/10.1017/S0263574712000446 Published online by Cambridge University Press

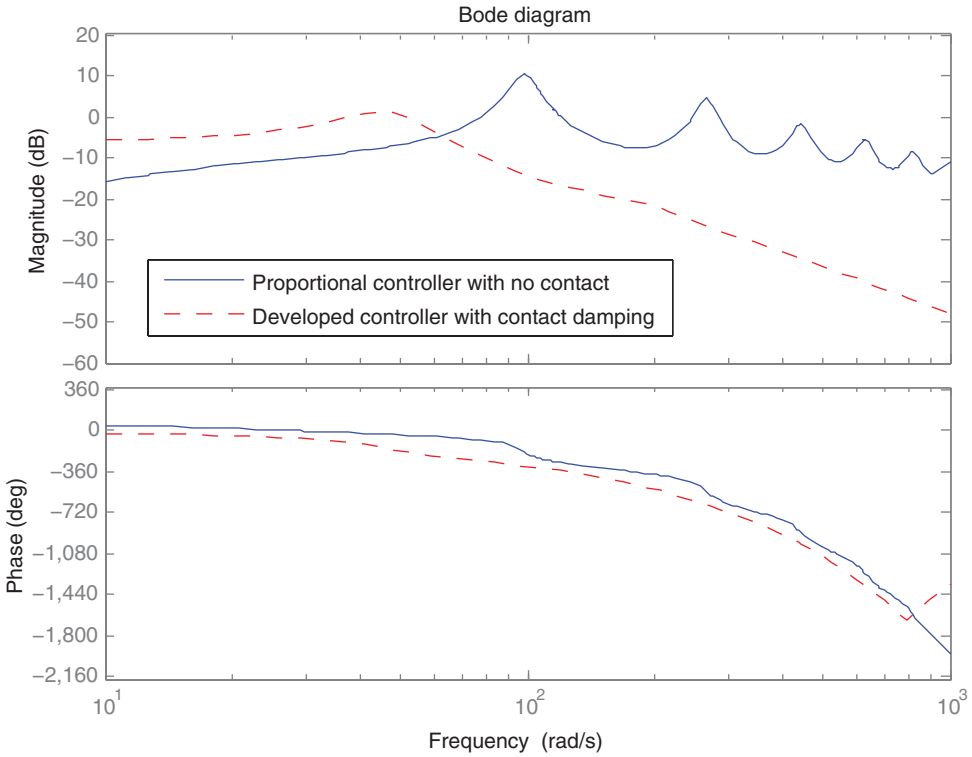


Fig. 7. (Colour online) Bode characteristic of the transfer function $G_Z(s)$ obtained through simulation. Frequency pertains to angular frequency and was expressed in $\frac{\text{rad}}{\text{s}}$, the magnitude pertains to amplitude and was expressed in dB.

produced by a simple multiplication of the noisy measured force F_m, while the measured velocity $\dot{X}_m$ is smooth due to the manipulator dynamics (relatively high inertia resulting in low pass filtration).

The graphs in Fig. 6 present the signals obtained from the MATLAB Simulink simulation. Figure 6(b) presents the simulation of F_d and F_m signals with two well-visible resonance peaks. Only the first of those peaks, which is much higher, was observed during the experiments. For both graphs in Fig. 6, the current frequency f_s of the desired signal is proportional to the current time of simulation t_s:

$$f_s = pt_s, \tag{8}$$

where $p = 1\ (\frac{\text{Hz}}{\text{s}})$ is the proportional factor. It should be noted that in principle the Bode characteristics were used to obtain the controlled plant parameter values.

The graph in Fig. 7, obtained for proportional controller with no contact, presents the Bode characteristics of the transfer function G_Z of the whole system presented in Fig. 3. Several resonance peaks are visible. From our point of view, the first one is important because it is dominating experimental results. For the resonant frequency of the investigated system, the phase shift $\mathcal{P}(G_Z) = -180^\circ$.

The graph in Fig. 8(a) presents the simulated Bode characteristics of G_{3I4} element. In the experiment, the transfer function G_{3I4} of the measured acceleration $\ddot{X}_m$ and the measured force F_m was also investigated for the resonant frequency of the whole control system. For this particular frequency the phase shift $\mathcal{P}(G_{3I4})$ is approximately -180°.

4. Force Regulator Development

Force control should attain low damping, in the sense described in Section 1, without oscillation in the assumed frequency band. On the basis of the previous experiments the first-order lag element $G_1(s) = \frac{\frac{1}{B_p}}{\frac{M_p}{B_p}s+1}$ was proposed as a force regulator. Then for the purpose of control system implementation, the developed continuous force regulator was transformed into a discrete form (Eq. (15)). The job of the proposed first-order lag element is to damp signals of frequencies starting around the frequency of the resonance peak, with adequately high gain for frequencies below the frequency of the resonance peak (Fig. 7).

To perform low pass filtration, the first-order lag element was chosen as a regulator, instead of PI regulator, commonly used in force feedback.[31] PI regulator constrains high-frequency response, and also integrates the systematic force measurement error, which cannot be removed. It can cause the manipulator to accelerate, when free motion is commanded (i.e., no contact occurs).

4.1. Discretization of the control law

For the purpose of the controller development, the signals shown in Fig. 3 are represented in continuous domain (s) and for the purpose of control law formulation in discrete domain (z). Hence, the force regulator block can be represented in three forms: discrete control law (the way it was implemented), discrete transform $G_1(z)$, and continuous transform $G_1(s)$.

To perform the initial identification experiments (Section 3), the discrete control law was formulated as a

https://doi.org/10.1017/S0263574712000446 Published online by Cambridge University Press

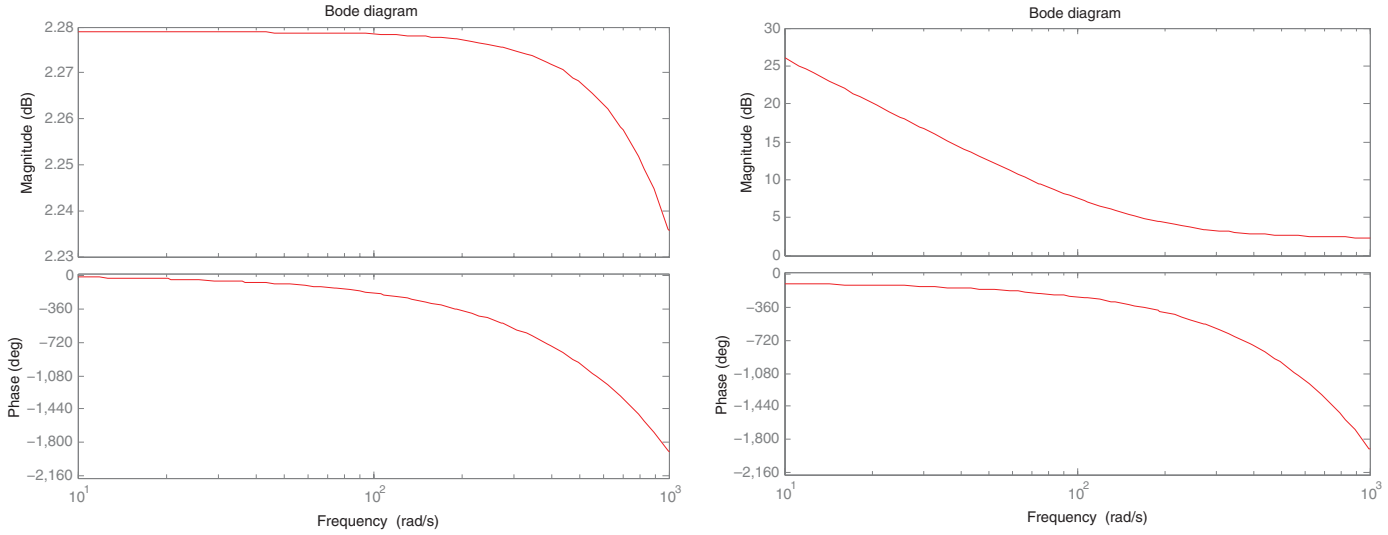


Fig. 8. (Colour online) Bode characteristic of transfer functions obtained through simulation. (a) $G_{3I4}(s)$ (the identification phase $B = 0$); (b) $G_{3I4}(s)$ (the increase of contact damping to $B = 200$).

damping control:

$$V_d^{\iota+1} = \frac{1}{B_p}\mathcal{F}_e^{\iota}, \tag{9}$$

where

$$\mathcal{F}_e^{\iota} = \mathcal{F}_d^{\iota+1} - \mathcal{F}_m^{\iota}, \tag{10}$$

where ι is the current time instant and $\iota + 1$ is the next time instant. The time instants are sampling time Δt apart. A similar approach (impedance-based indirect force control) was presented in ref. [26]. For the simple control law (Eq. (9)), $G_1'(z) = \frac{1}{B_p}$, and after transformation for the purpose of analysis into continuous domain, $G_1'(s) = \frac{1}{B_p}$. An adequately short sample period Δt was chosen to make this transformation valid. The identification experiments showed an approximately linear behavior of the plant. The analysis was performed (Section 4) and the first-order lag element

$$G_1(s) = \frac{\frac{1}{B_p}}{\frac{M_p}{B_p}s + 1} \tag{11}$$

was chosen as a force controller transfer function. The transmittance (Eq. (11)) can be transformed into the following discrete form:

$$G_1(z) = \frac{\frac{1}{B_p}\Delta t}{\frac{M_p}{B_p}(1 - z^{-1}) + \Delta t} \tag{12}$$

using a simple backward rectangular transformation:[6]

$$s = \frac{1 - z^{-1}}{\Delta t}. \tag{13}$$

The goal was to obtain a control law simple to implement, compute, and extend. Thus, transformation (Eq. (13)) was used instead of Tustin's method (bilinear transformation), producing more complex results. After some simple algebraic transformations of Eq. (12), the following equation used as a base for the final control law formulation can be written:

$$\left(\Delta t + \frac{M_p}{B_p}\right) z V_d(z) - \frac{M_p}{B_p} V_d(z) = \frac{1}{B_p}\Delta t\, z\mathcal{F}_e(z). \tag{14}$$

Finally, after some more transformations, the adjusted control law was obtained:

$$V_d^{\iota+1} = \frac{\frac{1}{B_p}\mathcal{F}_e^{\iota}\Delta t + \frac{M_p}{B_p} V_d^{\iota}}{\Delta t + \frac{M_p}{B_p}}. \tag{15}$$

The proposed control law (Eq. (15)) can be formulated individually for each of the six directions in the operational space because these directions are generally decoupled by using indirect kinematics problem solver of inverted Jacobian in indirect force control scheme. It should be noted that Δt should be small to make this assumption valid.

Table III. Force regulator development – values of control system parameters.

f_{r_e}	f_{r_s}	B_p	M_p	T_a	T_b	T_d	M	B	K
7.1	7.4	200	4	0.004	0.02	0.033	1.3	200	0

	G_1	G_2		G_{3I4}		G_{I4}	G_Z
	Exp, Sim	Exp	Sim	Exp	Sim	Sim	Sim
$\mathcal{L}()$	−49	−3	−2.8	14.8	13.1	13.1	1.3
$\mathcal{P}()$	−43	−52	−53	−170	−161	−74	−153

4.2. Setting of regulator parameter values

There is a heuristic rule of choosing the proposed regulator parameter values. For the contact with low damping (similarly low stiffness) or at no contact at all, it is possible to obtain low damping with high inertia, i.e., low value of B_p and high value of M_p are applied. It should be noted that introduction of such regulator properties produces low pass

https://doi.org/10.1017/S0263574712000446 Published online by Cambridge University Press

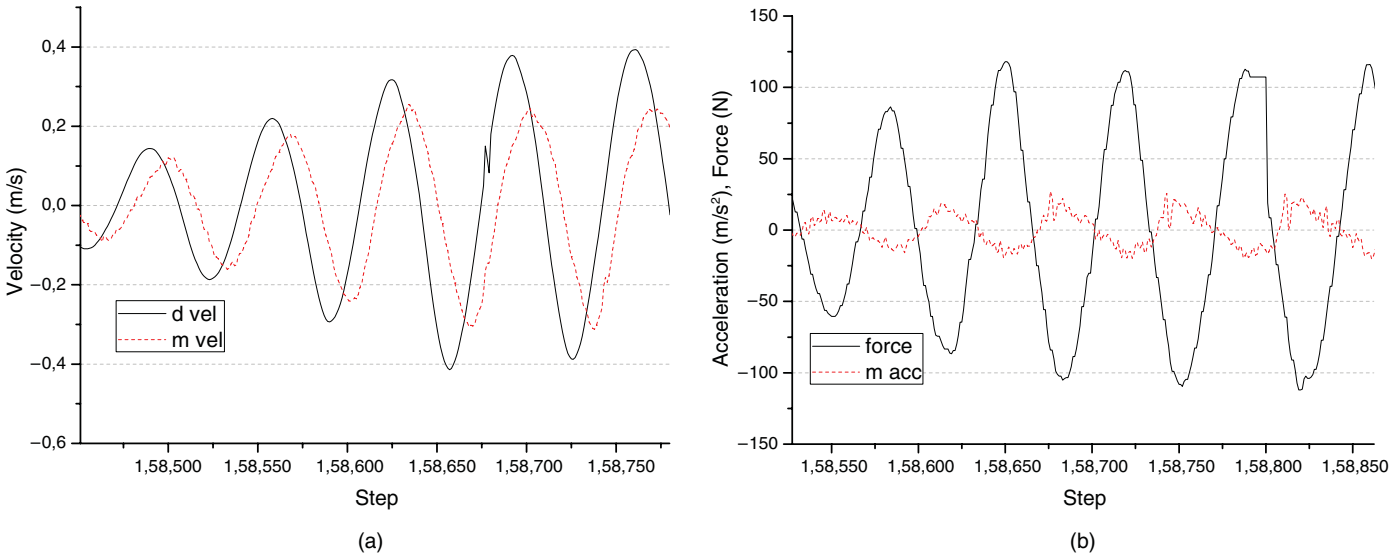


Fig. 9. (Colour online) Experiments for developed force regulator. (a) d vel – $\dot{X}_d$, m vel – $\dot{X}_m$; (b) m acc – $\ddot{X}_m$, force – F_m.

filteration and the resonance peak frequency drops (Table III and Fig. 9; the lowest in all of the experiments described in this paper). Hence, when high contact damping B occurs, there is a risk of noticeably low-frequency oscillations. For the contact with high damping or high stiffness there is a need to increase B_p, while M_p can stay low. Further experiments presenting the influence of regulator parameters on the contact behavior were performed for a haptic system.[28]

The major challenge was to estimate the contact properties before contact occurs. Alternatively, the contact current stiffness K_c can be computed to calculate force controller parameters while contact was maintained,[26] taking into account the relationship between measured position X_m and measured force $\mathcal{F}_m$ increments:

$$K_c^i = \begin{cases} \frac{\mathcal{F}_m^i - \mathcal{F}_m^{i-1}}{X_m^i - X_m^{i-1}} & \text{for } \operatorname{sgn}\left(\mathcal{F}_m^i - \mathcal{F}_m^{i-1}\right) = sgn\left(X_m^i - X_m^{i-1}\right) \\ K_c^{i-1} & \text{otherwise} \end{cases}, \tag{16}$$

where sgn is the signum, i is the time instant, and n_s is the natural factor:

$$i = \iota * n_s. \tag{17}$$

The computed stiffness should exceed zero to be valid, otherwise it simply remains as it was before. Both $\mathcal{F}_m^i$ and X_m^i were computed with respect to the current end-effector orientation. This method hardly depends on both position and force measurement accuracy and resolution, especially for low n_s values. In practice this concept was hard to apply for a typical industrial robot, hence we propose similar method based on the total stiffness concept presented in Section 6, applicable for contact of the manipulator end-effector with motionless objects in the environment.

5. Evaluation of Procedure

The evaluation of the proposed procedure started with the verification of correctness of controlled plant parameters identified previously in Section 3.2. Exemplary experiments with various B_p and B parameter values were presented in Section 5.1 ($B_p = 100$, $B = 0$), Section 5.2 ($B_p = 100$, $B = 100$), and Section 5.3 ($B_p = 200$, $B = 200$). Then the developed force controller was tested by a wide number of practical applications briefly enumerated in Section 5.4.

Table IV. Increase of force loop damping – values of control system parameters.

f_{r_e}	f_{r_s}	B_p	M_p	T_a	T_b	T_d	M	B	K
14.8	15.6	100	0	0.004	0.02	0.033	1.3	0	0

	G_1	G_2		G_{3I4}		G_{I4}	G_Z
	Exp, Sim	Exp	Sim	Exp	Sim	Sim	Sim
$\mathcal{L}()$	−40	−6	−7.5	2.3	2.3	2.3	1.4
$\mathcal{P}()$	0	−87	−84	−180	−186	0	−180

5.1. *Increase of regulator damping*

The following experiments were performed to verify the identified model and results were compared to those presented in Table II. At the beginning, the value of B_p was increased from 70 to 100, hence the gain of the force regulator was decreased. In the experiments the resonant frequency slightly decreased, but in simulation it did not. The range of change was small, did not significantly influence the system, and was neglected. In both experiments and simulation the decreased amplitude of oscillations was observed (the $\mathcal{L}(G_Z)$ value became smaller; Table IV).

5.2. *Introduction of contact*

When contact occurs (the tool was connected to a damper, e.g, an operator's hand, while the manipulator was oscillating), plots of the measured force F_m are considerably different from the plots obtained in the initial experiments, where only inertial force influenced the force measurement F_m. This phenomenon can be simulated by the introduction of contact

https://doi.org/10.1017/S0263574712000446 Published online by Cambridge University Press

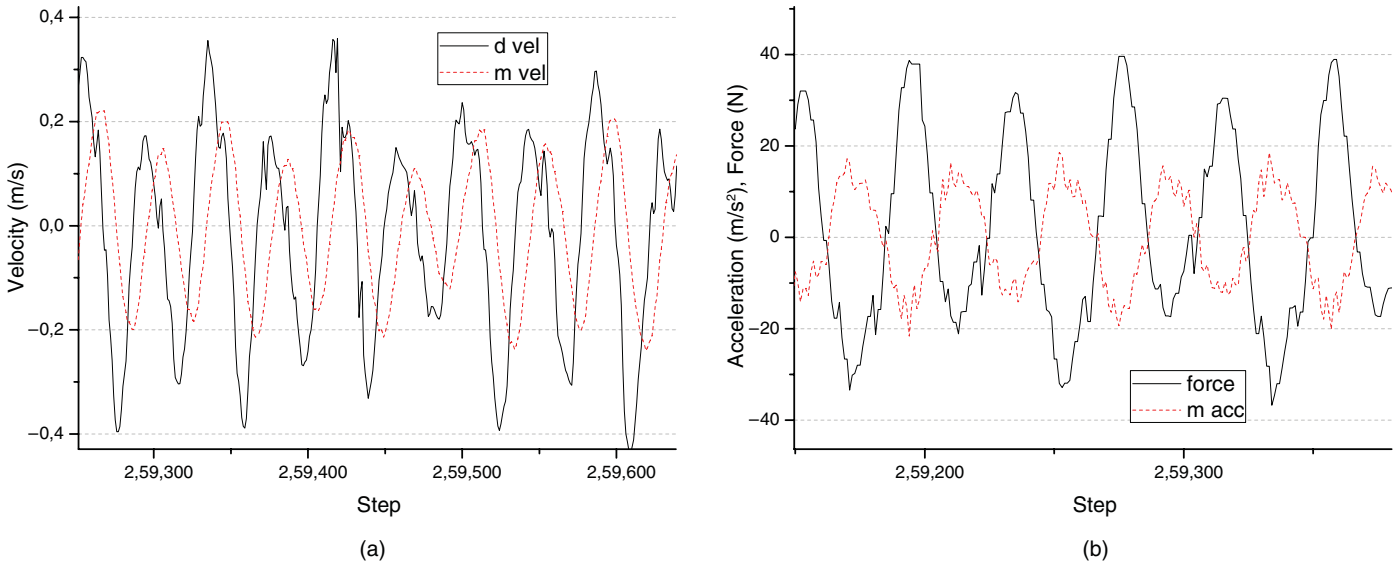


Fig. 10. (Colour online) Experiments when contact damping was introduced ($B = 100$). (a) d vel – $\dot{X}_d$, m vel – $\dot{X}_m$; (b) m acc – $\ddot{X}_m$, force – F_m.

damping (Fig. 10). The phase shift and gain between $\ddot{X}_m$ and F_m signals increased when contact damping was introduced. As a consequence the resonant frequency f_{r_e} decreased and the gain $\mathcal{L}(G_Z)$ increased (Table V). This phenomenon is visible in the following experiments (Figs. 11, 8(b)).

5.3. Increase of contact damping

In this stage of the procedure evaluation the force regulator damping value was set at $B_p = 200$ and to obtain oscillations the contact damping had to be increased to $B = 200$ (Table VI). The force regulator with high damping was relatively robust unless high contact damping occurred.[26]

The resonant frequency f_{r_e} decreased. There were two trends:

- Increase of contact damping B caused increase of resonance peak amplitude.

Table V. Introduction of contact damping in end-effector ($B = 100$) – values of control system parameters.

f_{r_e}	f_{r_s}	B_p	M_p	T_a	T_b	T_d	M	B	K
12.5	12.4	100	0	0.004	0.02	0.033	1.3	100	0

	G_1	G_2		G_{3I4}		G_{I4}	G_Z
	Exp, Sim	Exp	Sim	Exp	Sim	Sim	Sim
$\mathcal{L}()$	−40	−4	−5.8	5	5.2	5.2	8.7
$\mathcal{P}()$	0	−80	−75	−190	−193	−45	−170

- Increase of force regulator damping B_p caused decrease of resonance peak amplitude and slight decrease of resonant frequency.

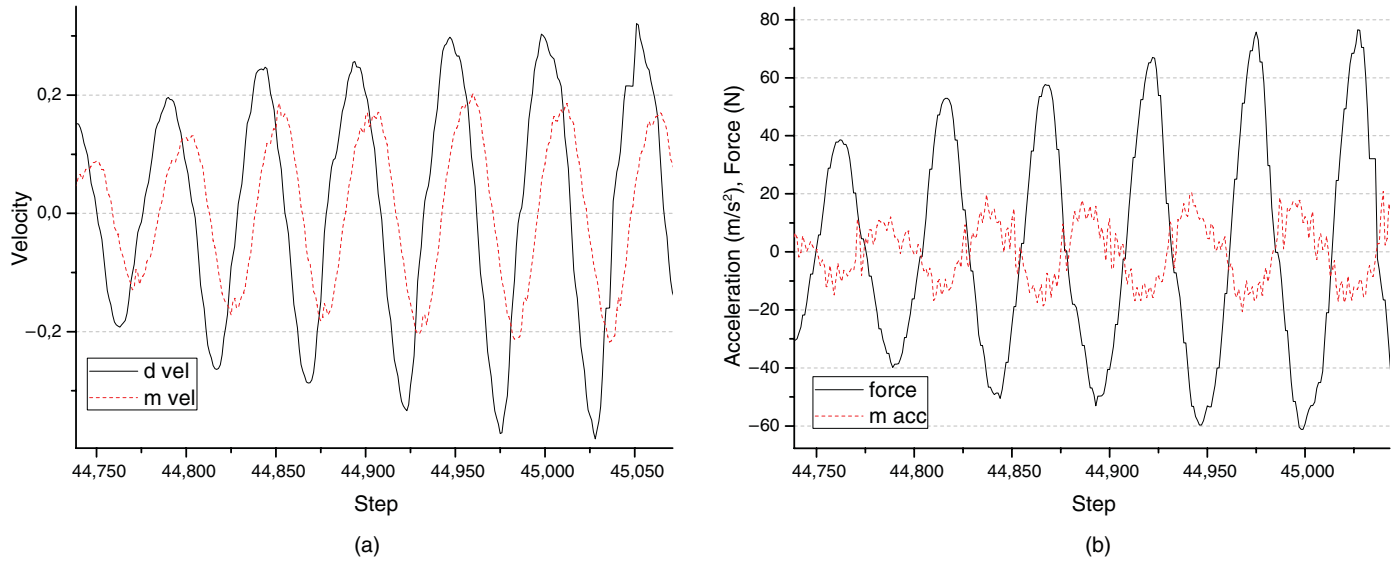
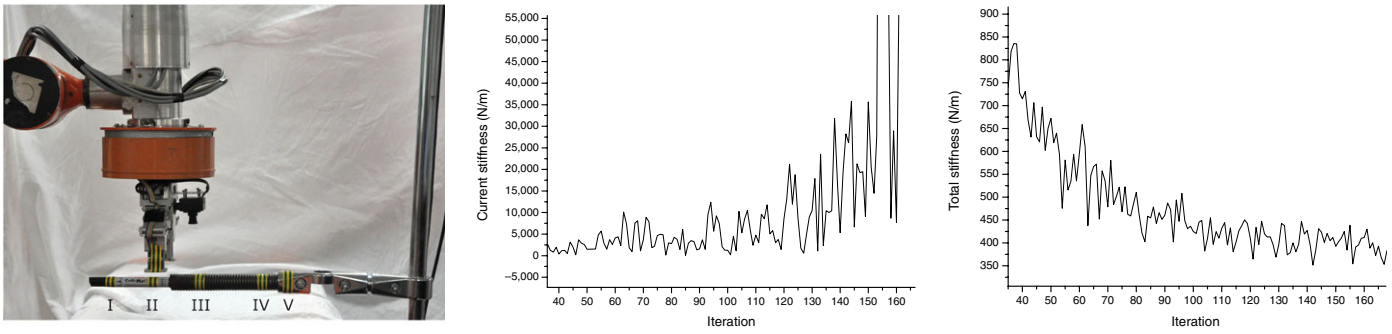


Fig. 11. (Colour online) Results of experiments with increase of contact damping to $B = 200$. (a) d vel – $\dot{X}_d$, m vel – $\dot{X}_m$; (b) m acc – $\ddot{X}_m$, force – F_m.

https://doi.org/10.1017/S0263574712000446 Published online by Cambridge University Press



(a) (b) (c)

Fig. 12. (Colour online) Experimental station and current and total stiffness exemplary waveforms. (a) End-effector approaching the spring; (b) current stiffness K_c after impact at the contact point II; (c) total stiffness K_t after impact at the contact point II.

Table VI. Increase of contact damping between end-effector and environment ($B = 200$) – values of control system parameters.

f_{r_e}	f_{r_s}	B_p	M_p	T_a	T_b	T_d	M	B	K
9.8	10.6	200	0	0.004	0.02	0.033	1.3	200	0

	G_1	G_2		G_{3I4}		G_{I4}	G_Z
	Exp, Sim	Exp	Sim	Exp	Sim	Sim	Sim
$\mathcal{L}()$	−46	−3.5	−4.8	10	10.2	10.2	4.2
$\mathcal{P}()$	0	−69	−68	−200	−194	−67	−160

In Fig. 11 the measured force F_m is less dependent on acceleration $\ddot{X}_m$ than in Fig. 10.

The Bode characteristics in Figs. 8(a) and (b) illustrate increase of magnitude of G_{3I4} element, with the introduction of high contact damping.

5.4. Applications test

The force controller was tested by a number of applications formally specified and presented in detail (including experiments[1,2]) in other papers of the authors: the following of an unknown contour and rotating the crank system,[33] parallel visual-force control system,[25] haptic coupling of two manipulator systems,[28] multi-robot system that copies drawings,[35] and Rubik's cube manipulation by a two-robot system.[36]

6. Contact Stiffness-Based Regulator Parameter Adaptation Method

The current section presents an approach to the development of an adaptive force controller in the form presented in Section 4 utilizing an experimental station described in Section 6.1. The proposed method started by a new formulation of the contact stiffness estimation algorithm for contact with motionless objects (Section 6.2). A number of experiments were performed to identify appropriate controller parameter values based on the computed contact stiffness (Section 6.3). Finally, the adaptation law was formulated (Section 6.4) that took into account previous experiments, and controller performance was experimentally verified (Section 6.5) for impact and contact with an environment of various stiffnesses.

6.1. Experimental station

The experiments were performed on a test rig presented in Fig. 12(a). For clearness of the presentation, we concentrate here on a single linear direction in operational space. The manipulator end-effector moved in the vertical direction (z-axis), impacted the horizontally mounted spring attached to a rigid pole, and tried to maintain contact with desired force $F_d = 10$N. Five contact points are labeled by roman numbers: "I" to "V". Generally, closer the contact occurs to the attachment point "V", higher is the stiffness of the spring.

The current stiffness K_c and the total stiffness K_t were identified in real-time experiments. It should be noted that stiffness is not only the stiffness of object but both manipulator and object in contact.

6.2. Contact stiffness estimation

The computation of stiffness, based on small increments of both force and position (Eq. (16)), is highly inaccurate. To solve this problem, a new method was developed. When the contact was detected, the "total" stiffness was estimated based on force and position increment in relation to measurement performed in time instant. Under these conditions, the increments were significantly higher and estimation was valuable.

The system started with total contact stiffness set to zero, i.e., $K_t^i = 0$. When the force exceeded certain threshold value, $\mathcal{F}_l$:

$$\left(\mathcal{F}_m^i > \mathcal{F}_l\right) \wedge \left(\mathcal{F}_m^{i-1} \leq \mathcal{F}_l\right), \tag{18}$$

it registered the initial contact force $\mathcal{F}_m^{i_0}$ and the initial contact position $X_m^{i_0}$ at the time instant i_0,

$$i = i_0, \quad \mathcal{F}_m^{i_0} = \mathcal{F}_m^i, \quad X_m^{i_0} = X_m^i. \tag{19}$$

The force threshold $\mathcal{F}_l$ should slightly exceed the force measurement noise level. The next step was to compute the total contact stiffness similar to the current stiffness, but taking into account the initial force and position.

$$K_t{}^i = \begin{cases} \frac{\mathcal{F}_m^i - \mathcal{F}_m^{i_0}}{X_m^i - X_m^{i_0}} & \text{for } [\text{sgn}(\mathcal{F}_m^i - \mathcal{F}_m^{i_0}) = \text{sgn}(X_m^i - X_m^{i_0})] \wedge \\ & [\text{abs}(\mathcal{F}_m^i - \mathcal{F}_m^{i_0}) > \mathcal{F}_b] \\ K_t^{i-1} & \text{otherwise} \end{cases}. \tag{20}$$

https://doi.org/10.1017/S0263574712000446 Published online by Cambridge University Press

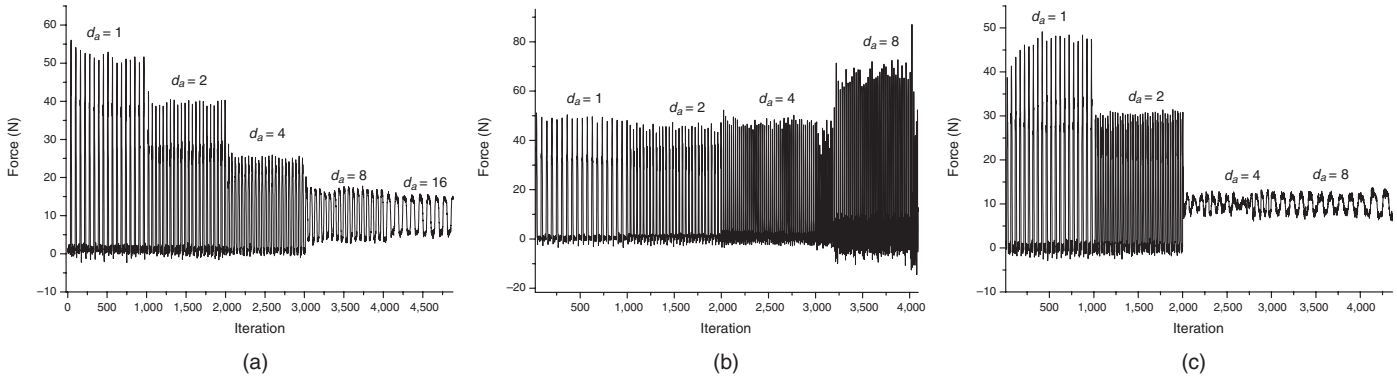


Fig. 13. Controller optimal parameters identification at contact point V. (a) $B_p = B_a \times d_a,\ M_p = M_a$; (b) $B_p = B_a,\ M_p = \frac{M_a}{d_a}$; (c) $B_p = B_a \times d_a,\ M_p = \frac{M_a}{d_a}$.

In addition, the force increment threshold $\mathcal{F}_b$ has to be exceeded to obtain the new stiffness estimation value. The $\mathcal{F}_b$ value depends on the force measurement noise and resolution. It should be noted that when the manipulator end-effector looses contact with the object, the procedure starts from the beginning. Figure 12 presents a significant difference in the total and current stiffness waveforms after impact at contact point II. The total stiffness stabilizes with increase in force, whereas the current stiffness varies significantly with time and increase.

6.3. Optimal controller parameters' identification

The proposed method was investigated for a particular IRb6 manipulator. The procedure presented in Sections 3 and 4 led to the setting of force controller parameters to $B_p = 100$ and $M_p = 40$ for free motion. Especially the inertia value was set high to achieve robustness when the manipulator end-effector moved without contact with the environment. The experiments were performed for all of the contact points. Later on the results for three representative points were presented. The total stiffness ($\frac{\mathrm{N}}{\mathrm{m}}$) estimated during experiments was: 500 to 1,000 for contact point II, 1,500 to 2,500 for contact point III, and 15,000 to 25,000 for contact point V. The desired force was constantly set as follows: $F_d = 10$(N) and force sensitivity level, $\mathcal{F}_l = 1$ (N). It should be noted that we decided not to filter force signal to achieve fast reaction to impact.

Factor d_a was introduced to influence force controller parameters. It started from 1 and is multiplied by 2 every 1,000 iterations. The general concept was to find the lowest factor achieving stable contact. Figure 13 presents three experiments performed with different influence of d_a on controller parameters (see the labels of the particular Figs. 13(a)–(c)). It seems to be clear that simultaneous influence on both damping and inertia leads to the best controller performance for $d_a = 4$, while the end-effector starts to maintain contact without loosing it. It should be noted that the strategy of changing inertia without increasing damping leads to serious instability.

For other contact points, the best strategy is presented in Fig. 14. Similar to contact point V, at contact point III, factor $d_a = 4$ is the lowest to achieve low-amplitude oscillations. At contact point II, adaptation does not influence force measurement significantly, so factor $d_a = 1$ seems to be valid.

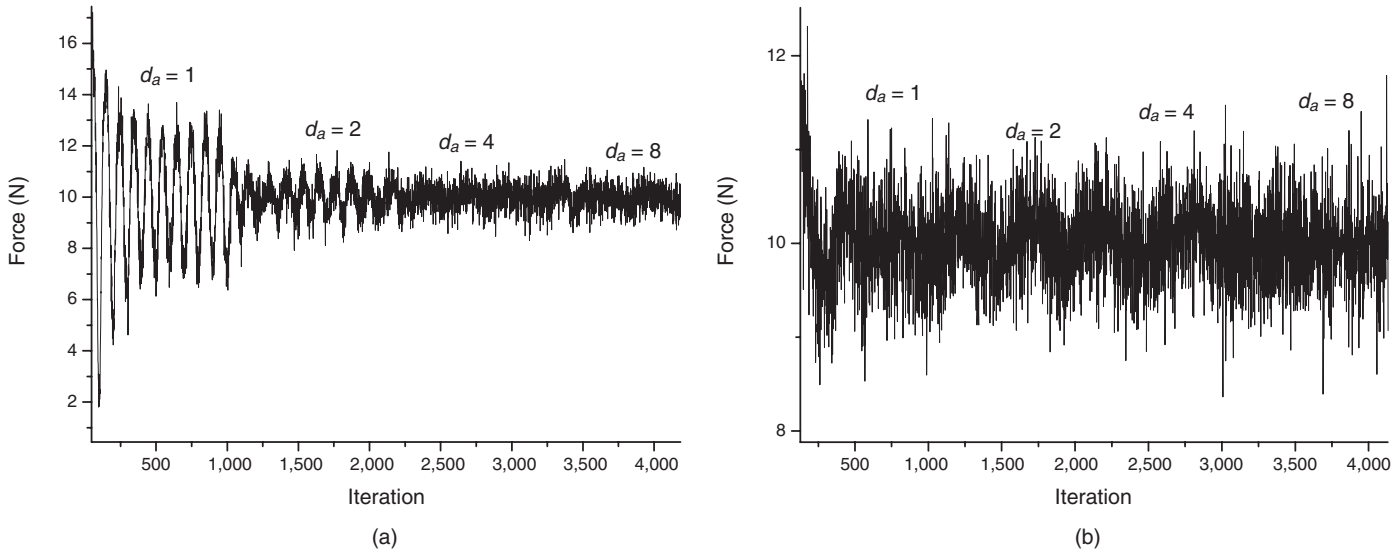


Fig. 14. Controller optimal parameters identification at contact points III and II with increasing damping and decreasing inertia: $B_p = B_a \times d_a,\ M_p = \frac{M_a}{d_a}$. (a) Contact point III; (b) contact point II.

https://doi.org/10.1017/S0263574712000446 Published online by Cambridge University Press

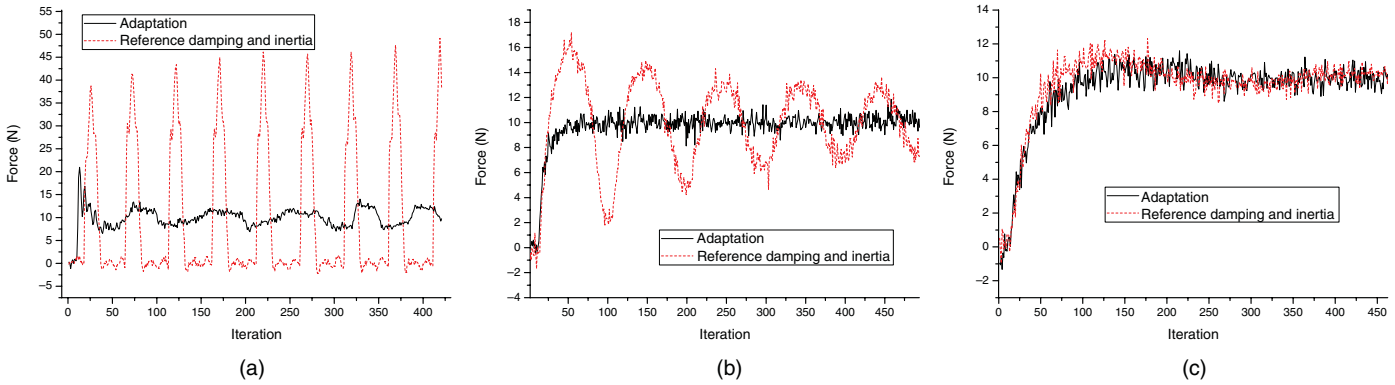


Fig. 15. (Colour online) The reference and adaptive controllers' behavior after impact on spring at contact points V, III, and II. (a) Contact point V; (b) contact point III; (c) contact point II.

6.4. Adaptation of law formulation

Controller parameter adjustment was based on the value of total stiffness K_t. The previous work[28] leads to the conclusion that in general for high K_t values, M_p should be lowered and B_p should become higher than for low K_t values. In this paper (Section 6.3), we investigated contact properties to develop the control law. We assumed that both parameters, M_p and B_p, should be modified by the same factor d_a (Eq. (21)),

$$d_a = \begin{cases} 1 & \text{for } K_t < K_l \\ 1 + \frac{(K_t^i - K_l)(d_h - 1)}{K_h - K_l} & \text{for } (K_t \geq K_l) \wedge (K_t \leq K_h) \\ d_h & \text{for } K_t > K_h \end{cases}. \tag{21}$$

Factor $d_a = 1$ for low stiffness values (lower then K_l), then it linearly increases to reach maximum value d_h for the upper stiffness limit K_h. The experiments lead to the following values of parameters: $K_l = 500$, $K_h = 2,000$, $d_h = 4$.

The controller parameter modification algorithm was as follows:

$$B_p = B_a \times d_a, \qquad M_p = \frac{M_a}{d_a}, \tag{22}$$

where $M_a = 40$ is the reference inertia, and $B_a = 100$ is the reference damping.

6.5. Verification

Finally, the adaptation algorithm was compared with the reference controller (with constant parameter values: $B_p = 100$ and $M_p = 40$), while the manipulator end-effector impacted spring at three representative contact points with various stiffnesses (Fig. 15). At contact point V the adaptive controller leads to stable contact maintenance while reference controller looses contact with stiff environment. At contact point III the adaptive controller removes low-frequency oscillations (high-frequency oscillations are caused by measurement noise). The behavior of both algorithms is the same at contact point II because the adaption factor $d_a = 1$ for low contact stiffness. The experiments positively verify the proposed adaptation approach based on the total stiffness estimation.

7. Conclusions

Indirect force control is suitable for controlling majority of the typical industrial manipulators equipped additionally with a force transducer in their wrists. These manipulators have often non-back drivable gears that makes direct force control nearly impossible. Indirect force control uses force controller implemented in the operational space, which is situated on the top of position controllers working in the joint space. The force controller development procedure should consider the identification of manipulator parameters (together with position servos), force sensor properties, and the properties of contact between the manipulator end-effector and the environment. The method presented in this paper uses both identification experiments and identified model analysis. Identification experiments were based on resonance phenomenon. The method is fast and can be easily applied by engineers. It is extended to a multidimensional position-force controller[36] and practically verified on IRb6 – a typical industrial serial manipulator. IRb6 can be equipped with a force sensor to produce new sensor-based applications without need to buy expensive new hardware and perform elaborated analysis and experiments. It significantly decreases the cost of introducing a modern production process. The same approach can be used to develop service robots.

Although the proposed control law is general in nature and robust, what has been verified by a wide range of practical applications (Section 5.4), the controller parameters' selection method used in this work can be extended. This method is qualitative and based on the previously assumed behavior of contact of the manipulator end-effector and the environment (Section 4). Alternatively, the parameters are computed based on the estimated contact stiffness for contact with motionless objects (Section 6). Further work will concentrate on the development of automatic algorithms for control law parameters' computation based on the estimation of contact impedance with object that is being contacted and supposed to be moved. For this purpose a precise multi-axis acceleration measurement in the manipulator end-effector is needed to filter out the majority of non-contact forces.[18] There are also other ways to increase the robustness of the force control, e.g., based on the virtual environment concept.[13]

https://doi.org/10.1017/S0263574712000446 Published online by Cambridge University Press

Acknowledgments

The authors gratefully acknowledge the support of the Ministry of Science and Higher Education grant N514 1287 33. The authors would like to thank Prof. Cezary Zieliński for his comments.

References

1. T. Winiarski and C. Zieliński, Position/force control with IRb6 manipulators under supervision of MRROC++ www.youtube.com/watch?v=R2zwEaxyhY0 (2011) (accessed August 1, 2012).
2. T. Winiarski and M. Staniak, Rubik's Cube solving with IRb6 manipulators under supervision of MRROC++ www.youtube.com/watch?v=wJpFcy99Gh0 (2011) (accessed August 1, 2012).
3. MRROC++ www repository. Available at: http://github.com/wut-rcprg/mrrocpp (2012), online (accessed August 1, 2012).
4. M. H. Ang Jr., "Towards pervasive robotics: Compliant motion in human environments," *Int. J. Softw. Eng. Knowl. Eng.* **15**(2), 135–145 (2005).
5. S. Arimoto, "Fundamental problems of robot control: Part I, innovations in the realm of robot servo-loops," *Robotica* **13**(01), 19–27 (1995).
6. K. J. Åström and B. Wittenmark, *Computer-Controlled Systems* (Prentice-Hall, Upper Saddle River, NJ, 1997).
7. S. Bennett, *A History of Control Engineering, 1800–1930* (Institution of Electrical Engineers Stevenage, UK, 1979).
8. H. Bruyninckx and J. De Schutter, "Specification of force-controlled actions in the task frame formalism: A synthesis," *IEEE Trans. Robot. Autom.* **12**(4), 581–589 (Aug. 1996).
9. R. Carelli, E. Oliva, C. Soria and O. Nasisi, "Combined force and visual control of an industrial robot," *Robotica* **22**(2), 163–171 (2004).
10. Y. Chen, "Implementation of a Lag-Lead Compensator for Robots." **In**: *Proceedings of the 27th IEEE Conference on Decision and Control*, Austin, Texas, USA (1988) pp. 174–179.
11. P. Dorato, "A historical review of robust control," *IEEE Control Syst. Mag.* **7**(2), 44–47 (1987).
12. W. Findeisen, *Grundlagen des Entwurfs von Regelungssystemen* (VEB Verlag Technik, Berlin, Germany, 1973).
13. P. Fraisse, P. Dauchez and F. Pierrot, "Robust force control strategy based on the virtual environment concept," *Adv. Robot.* **21**(3–4), 485–498 (2007).
14. T. Horie, K. Tanaka, N. Abe and H. Taki, "Remote Force Control of Robot Using PHANToM Haptic Model and Forcesensor," **In**: *Proceedings of the IEEE International Symposium on Assembly and Task Planning*, Fukuoka, Japan (2001) pp. 128–135.
15. S. Huang and J. M. Schimmels, "Admittance selection for force-guided assembly of polygonal parts despite friction," *IEEE Trans. Robot.* **20**(5), 817–829 (October 2004).
16. S.H. Jeong, T. Takahashi and E. Nakano, "A Safety Service Manipulator System: The Reduction of Harmful Force by a Controllable Torque Limiter," **In**: *Proceedings of the IEEE/RSJ International Conference on Intelligent Robots and Systems (IROS)*, Sendal, Japan, vol. 1 (2004) pp. 162–167.
17. O. Khatib, "A unified approach for motion and force control of robot manipulators: The operational space formulation," *Int. J. Robot. Autom.* **RA-3**(1), 43–53 (Feb. 1987).
18. T. Kroger, D. Kubus and F. M. Wahl, "Force and acceleration sensor fusion for compliant manipulation control in 6 degrees of freedom," *Adv. Robot.* **21**(14), 1603–1616 (2007).
19. K. J. Kurman, *Feedback Control: Theory and Design* (Elsevier Science, New York, NY, 1984).
20. T. E. Marlin, *Process Control: Designing Processes and Control Systems for Dynamic Performance* (McGraw-Hill, New York, 1995).
21. M. Mason, "Compliance and force control for computer controlled manipulators," *IEEE Trans. Syst. Man Cybern.* **11**(6), 418–432 (1981).
22. W. Meeussen, M. Wise, S. Glaser, S. Chitta, C. McGann, P. Mihelich, E. Marder-Eppstein, M. Muja, V. Eruhimov and T. Foote, *et al.*, "Autonomous Door Opening and Plugging in with a Personal Robot," **In**: *Proceedings of the IEEE International Conference on Robotics and Automation (ICRA)*, Anchorage, Alaska, USA (2010) pp. 729–736.
23. H. Seraji, "Adaptive Admittance Control: An Approach to Explicit Force Control in Compliant Motion," **In**: *Proceedings of the IEEE International Conference on Robotics and Automation*, San Diego, California, USA, Vol. 4 (May 1994) pp. 2705–2712.
24. M. Strolz and M. Buss, "Haptic rendering of actuated mechanisms by active admittance control," *Lecture Notes Comput. Sci.* **5024**, 712 (2008).
25. M. Staniak, T. Winiarski and C. Zieliński, "Parallel Visual-Force Control," *Proceedings of the IEEE/RSJ International Conference on Intelligent Robots and Systems (IROS '08)*, Nice, France (2008).
26. T. Tsumugiwa, R. Yokogawa and K. Hara, "Variable Impedance Control Based on Estimation of Human Arm Stiffness for Human-Robot Cooperative Calligraphic Task," **In**: *Proceedings of the 2002 IEEE Conference on Robotics and Automation*,Washington D.C., USA, Vol. 1 (May 2002), pp. 644–650.
27. M. Walęcki, K. Banachowicz and T. Winiarski, "Research-oriented motor controllers for robotic applications," *Lecture Notes Control Inf. Sci.* **422**, 193–203 (2012).
28. T. Winiarski and C. Zieliński, "Specification of multi-robot controllers on an example of a haptic device," *Lecture Notes Control Inf. Sci.* **396**, 227–242 (2009).
29. A. Woźniak, W. Szynkiewicz and C. Zieliński, "Robot controller with a self-measurement capability enabling the identification of friction," *Arch. Control Sci.* **13**(4), 391–414 (2003).
30. N. Zemiti, G. Morel, T. Ortmaier and N. Bonnet, "Mechatronic design of a new robot for force control in minimally invasive surgery," *IEEE/ASME Trans. Mechatronics* **12**(2), 143–153 (2007).
31. G. Zeng and A. Hemami, "An overview of robot force control," *Robotica* **15**, 473–482 (1997).
32. C. Zieliński, "Transition-Function Based Approach to Structuring Robot Control Software," **In**: *Robot Motion and Control: Recent Developments*, Lecture Notes in Control and Information Sciences, Vol. 335 (K. Kozłowski, ed.) (Springer Verlag, New York, 2006) pp. 265–286.
33. C. Zieliński, W. Szynkiewicz and T. Winiarski, "Applications of MRROC++ Robot Programming Framework," **In**: *Proceedings of the 5th International Workshop on Robot Motion and Control (RoMoCo'05)*, Dymaczewo, Poland (K. Kozłowski, ed.) (Jun 23–25 2005), pp. 251–257.
34. C. Zieliński, W. Szynkiewicz, T. Winiarski, M. Staniak, W. Czajewski and T. Kornuta, "Rubik's cube as a benchmark validating MRROC++ as an implementation tool for service robot control systems," *Ind. Robot Int. J.* **34**(5), 368–375 (2007).
35. C. Zieliński and T. Winiarski, "General specification of multi-robot control system structures," *Bull. Pol. Acad. Sci. Techn. Sci.* **58**(1), 15–28 (2010).
36. C. Zieliński and T. Winiarski, "Motion Generation in the MRROC++ Robot Programming Framework," *Int. J. Robot. Res.* **29**(4), 386–413 (2010).

https://doi.org/10.1017/S0263574712000446 Published online by Cambridge University Press